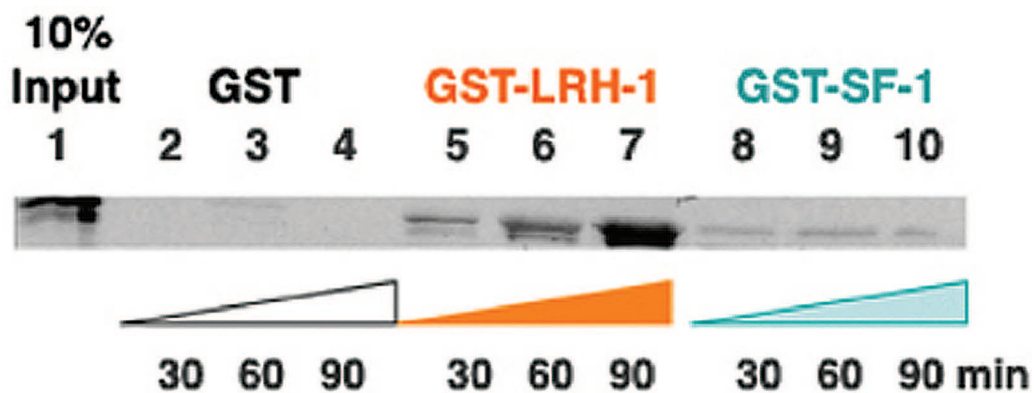


# Supporting Information

Sablin *et al.* 10.1073/pnas.0808936105



**Fig. S1.** GST pull-down assays showing a strong interaction between Dax-1 and LRH-1. GST fusion proteins containing LRH-1 and SF-1 LBDs were incubated with *in vitro* transcribed and translated <sup>35</sup>S full-length mDax-1 for 30, 60, and 90 min at room temperature. For each time point, the amount of Dax-1 bound to GST control protein (lanes 2–4), GST-LRH-1 LBD (lanes 5–7), or GST-SF-1 LBD (lanes 8–10) was determined, as shown in comparison to 10% of total Dax-1 input (lane 1). Bound proteins were resolved by SDS-PAGE and visualized by autoradiography. Different expression time points for <sup>35</sup>S-Dax-1 (30, 60, and 90 min) were used to determine whether the total amount and concentration of accumulated protein affected its binding interactions with the protein partners tested.



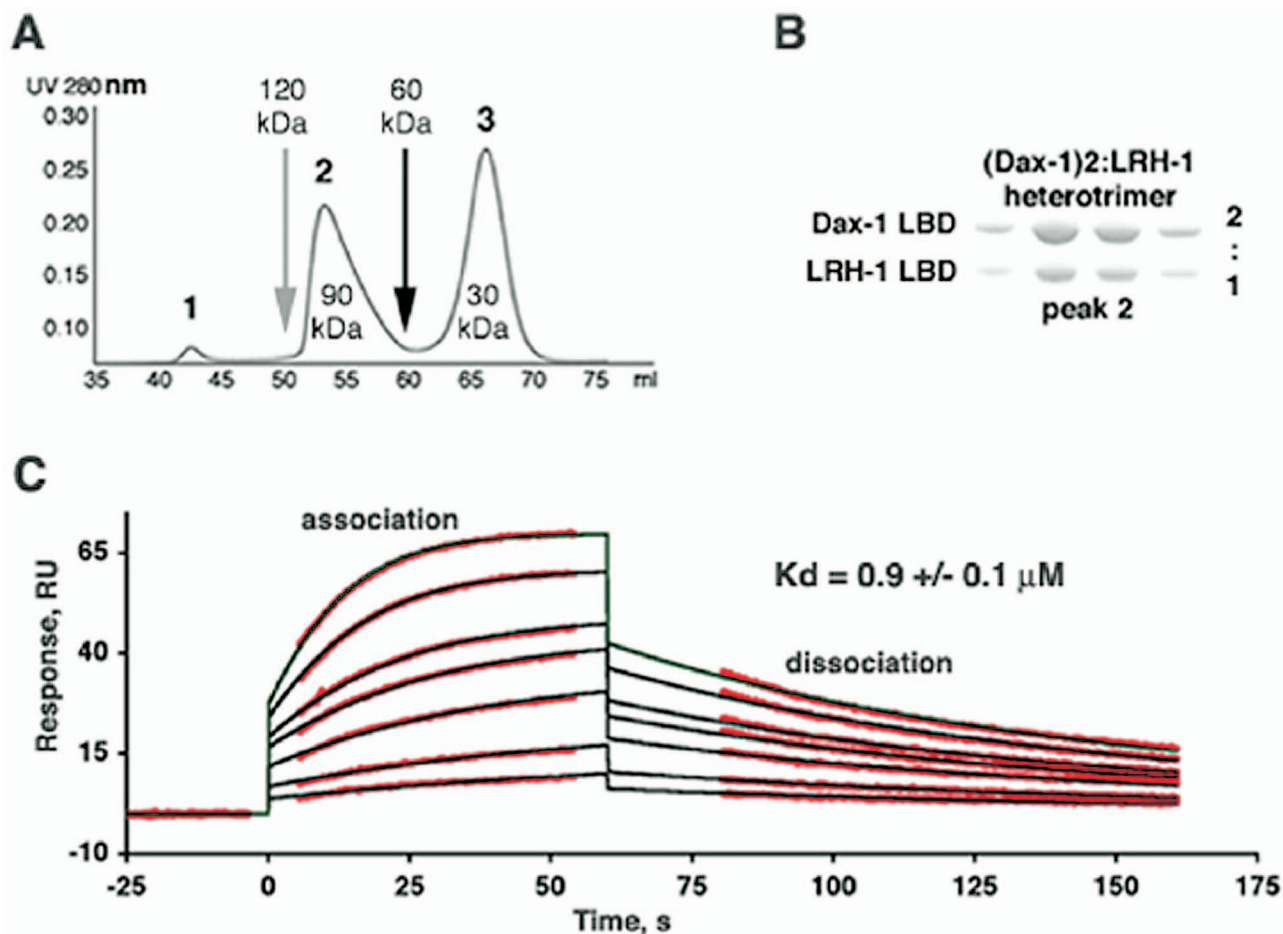


**Fig. S3.** Biochemical characterization of the (Dax-1)<sub>2</sub>:LRH-1 heterotrimer. (A) Size-exclusion chromatography of the (Dax-1)<sub>2</sub>:LRH-1 heterotrimer. An FPLC Supedex 75 HiLoad 16/60 column was calibrated using different nuclear receptor LBD monomers, homodimers and heterodimers, and tetramers. Retention volumes corresponding to a nuclear receptor LBD dimer (60 kDa) and tetramer (120 kDa) are indicated by black and gray arrows, respectively. Peak 3 represents the LRH-1 LBD monomer (30 kDa). Based on this calibration, peak 2 (90 kDa) corresponds to the (Dax-1)<sub>2</sub>:LRH-1 heterotrimer. The complex maintains its trimeric monodispersed state at low (0.1 mg/ml;  $\approx 1 \mu\text{M}$ ) and high (10 mg/ml;  $\approx 100 \mu\text{M}$ ) concentrations, suggesting an association with a  $K_d < 1 \mu\text{M}$ . (B) SDS-PAGE of the purified (Dax-1)<sub>2</sub>:LRH-1 heterotrimer. The analyzed protein sample corresponds to peak 2 in (A). Note the 2:1 ratio between the Dax-1 (*Upper*) and LRH-1 (*Lower*) components of the complex on the gel. (C) Surface plasmon resonance sensorgrams showing the formation and dissociation of the (Dax-1)<sub>2</sub>:LRH-1 complex. Samples of the Dax-1 protein (aa 205–472) at concentrations of 0.5, 1, 2, 4, 6, and 8  $\mu\text{M}$  were injected over the His<sub>6</sub>-tagged LRH-1 LBD immobilized on an Ni<sup>2+</sup> tri-NTA chip. The sensorgrams were corrected against responses over a blank reference surface, as well as against responses to injections of the 0  $\mu\text{M}$  Dax-1 samples. The experimental curves (with sharp transients and spikes removed) and fitted curves (for the one LRH-1 to one Dax-1 dimer binding model) are shown in black and red, respectively. The association and dissociation phases and the calculated equilibrium dissociation constant ( $K_d$ ) for the complex are indicated.

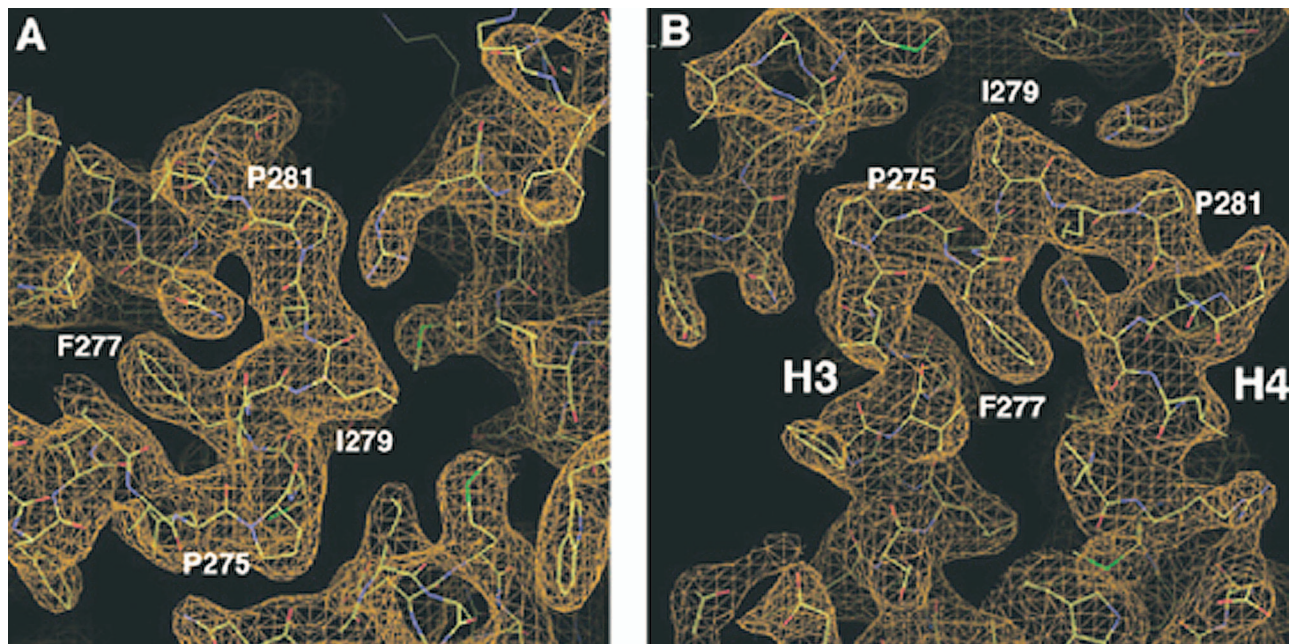


**Fig. S4.** Electron densities from a simulated annealing composite omit map for the (Dax-1)<sub>2</sub>:LRH-1 structure. (A) The repression helix of Dax-1 docked into the primary AF-2 site of LRH-1. (B) A different view of the Dax-1 repression helix, showing the preceding and following helices, H3 and H4. For both figures, the electron density (shown as gold mesh) is displayed at a contour level of  $1\sigma$ . Residues P275, F277, I279, and P281 from the Dax-1 repression helix are indicated. Note that both the main and the side chains of the complex are well defined by the density. As reported in [Table S1](#), the average temperature factor for the (Dax-1)<sub>2</sub>:LRH-1 structure is  $\approx 65 \text{ \AA}^2$ . In considering the source of the apparently high B values, we suggest that this is best explained by the limited crystal contacts, which allow rigid body vibrations of the otherwise well-ordered Dax-1 and LRH-1 domains. This reasoning is consistent with the fact that the refinement statistics for the structure can be further improved when the TLS option accounting for anisotropic rigid body domain motions (CCP4 program REFMAC) is used in the refinement. Because the individual temperature factors for the (Dax-1)<sub>2</sub>:LRH-1 structure do not display any large fluctuations and are distributed uniformly around  $65 \text{ \AA}^2$ , the electron density is well defined for all parts of the structure, as shown here.



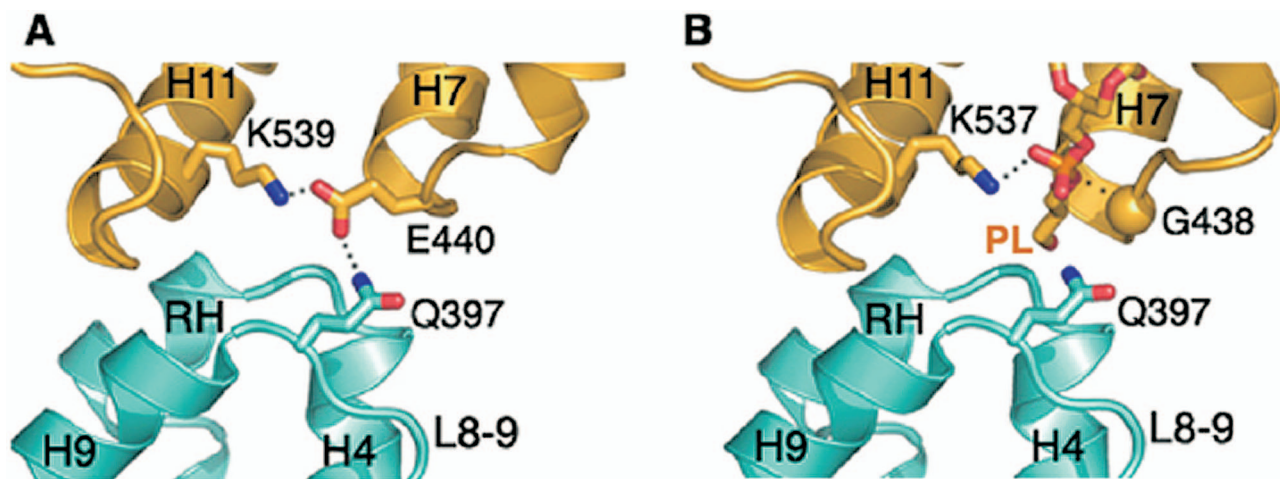


**Fig. S6.** A magnified view of the second Dax-1 (blue)–LRH-1 (yellow) interface, showing the major structural elements. (A) A fragment of the complex structure in the vicinity of the LRH-1 ligand-binding pocket. The position of the second Dax-1 LBD in the complex places the side chain of semiconserved Q397 in loop L8–9 of Dax-1 at the distance of direct contact with the residues at the entrance to the ligand-binding pocket of LRH-1, which in rodent LRH-1 is gated by a salt bridge formed between conserved K539 and E440 (indicated). (B) Modeling of human LRH-1 LBD into the (Dax1)<sub>2</sub>:LRH-1 heterotrimer. The structure of human LRH-1 LBD (pdb id 1Y0K) was superimposed with the mLRH-1 from the trimer. In the human structure, the exposed head of the bound phospholipid (shown as a stick model and denoted as “PL”) would replace the salt bridge and assume the same position in the three-dimensional space (indicated). Considering the existence of possible natural ligands for LRH-1, the placement of Dax-1 loop L8–9 in the vicinity of the LRH-1 ligand-binding pocket makes this loop a plausible candidate for a “sensor” of the LRH-1 ligand state and suggests that binding of the second Dax-1 might be controlled by a bound LRH-1 ligand *in vivo*.

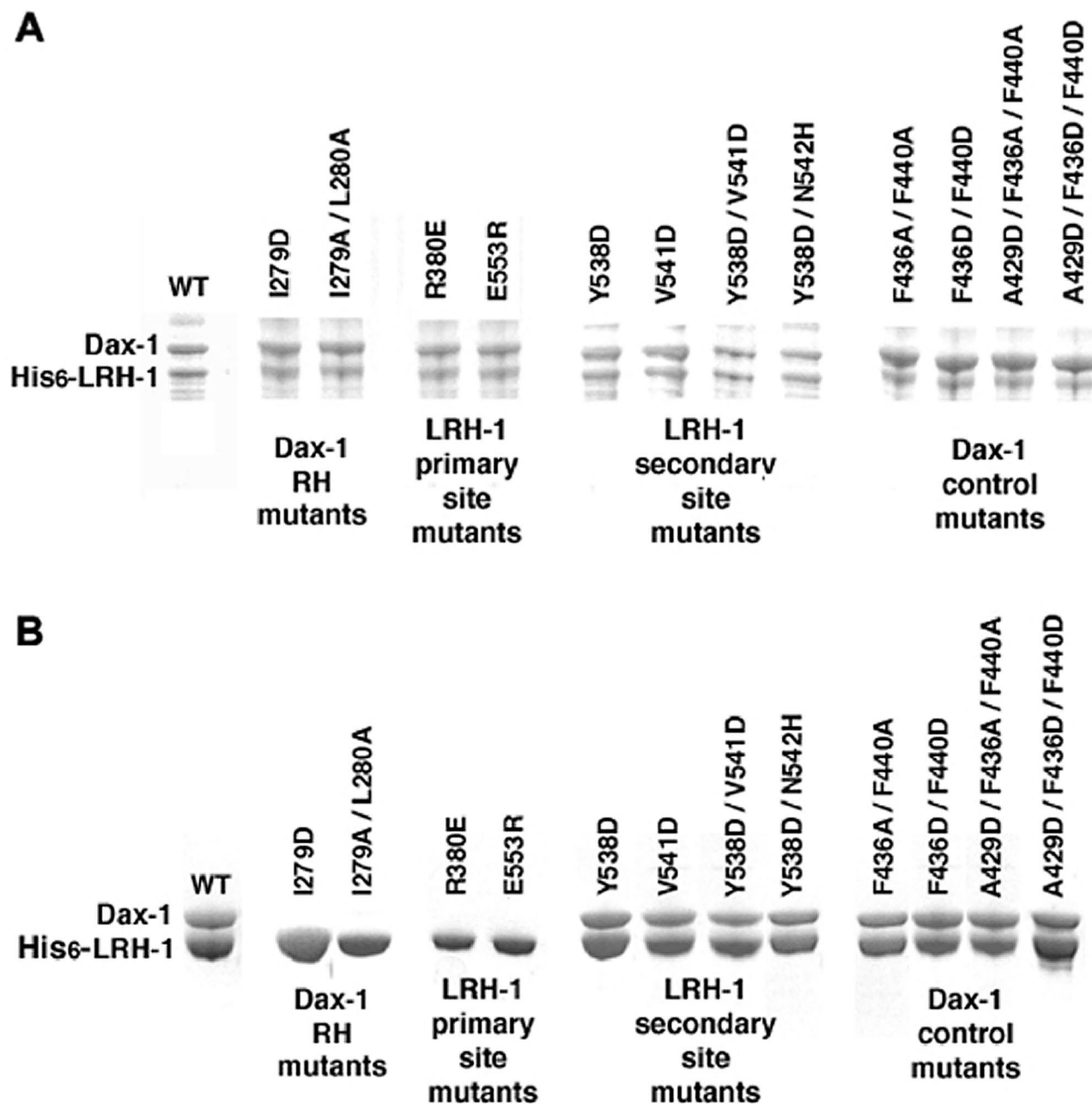


**Fig. S7.** Effects of mutations at Dax-1-LRH-1 interfaces on the binding of Dax-1 to LRH-1. (A) Coexpressed wild-type and mutant Dax-1 LBD and His<sub>6</sub>-tagged LRH-1 LBD proteins detected by SDS-PAGE in the soluble fractions of bacterial lysates. Dax-1 RH and LRH-1 primary and secondary site mutants are expressed at comparable levels to those of wild-type proteins. (B) SDS-PAGE of proteins bound to the affinity Ni-NTA matrix. Wild-type Dax-1 is associated and copurified with His<sub>6</sub>-tagged LRH-1 LBD. Dax-1 RH mutants do not bind to LRH-1. Similarly, single mutations at the LRH-1 primary binding site completely abolish Dax-1 binding. In contrast, mutations at the LRH-1 secondary binding site permit binding. Dax-1 control mutations do not affect the binding between Dax-1 and LRH-1.

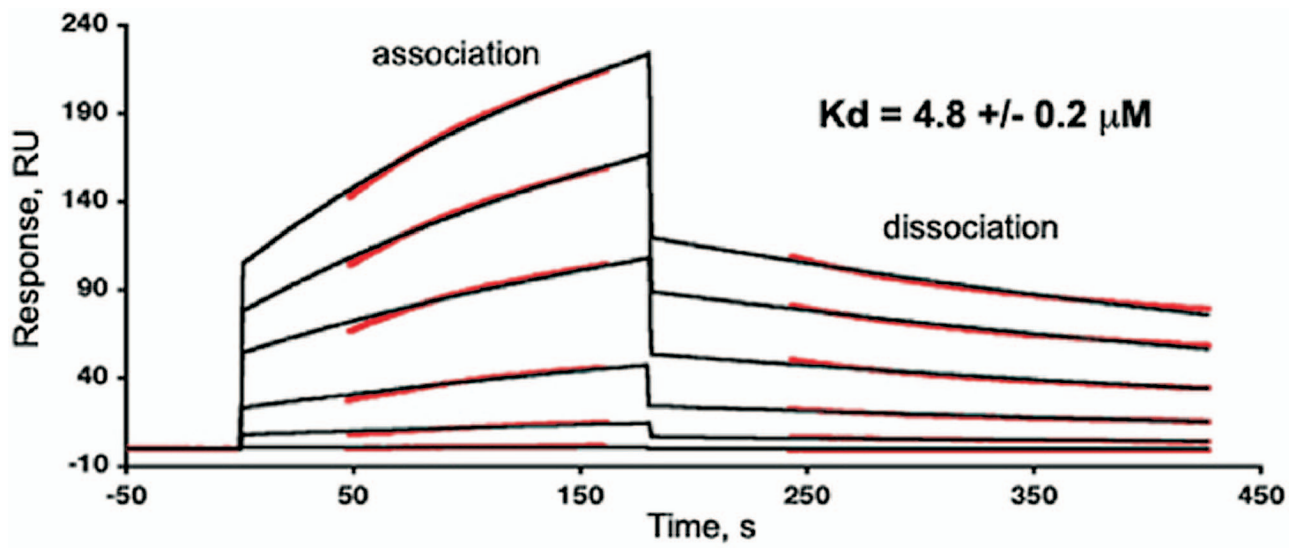


Fig. S8. SPR sensorgrams showing binding of the Dax-1 monomer to the LRH-1 LBD. Samples of the Dax-1 protein (aa 245–472) at concentrations of 0.5, 1, 2, 4, 6, 8, and  $\mu\text{M}$  were injected over the GST-tagged LRH-1 LBD immobilized on an anti-GST chip. Sensorgrams were corrected against responses over a blank reference surface, as well as against responses to injections of 0  $\mu\text{M}$  Dax-1 samples. The experimental curves (with sharp transients and spikes removed) and fitted curves (for the one-to-one binding model) are shown in black and red, respectively. The association and dissociation phases and the calculated equilibrium dissociation constant ( $K_d$ ) for the complex are indicated.

**Table S1. Data collection and refinement statistics**

Crystallization	
Unit cell dimensions	
<i>a</i> , Å	103.3
<i>b</i> , Å	103.3
<i>c</i> , Å	117.4
Space group	<i>P4</i> <sub>3</sub>
Molecules per asymmetric unit	1 (Dax-1) <sub>2</sub> :LRH-1 heterotrimer
Resolution, Å	3.0
Number of unique reflections	24,369
Completeness, %*	98.4 (96.9)
Data redundancy*	6.0 (3.5)
$\langle I/\sigma(I) \rangle^*$	18.4 (2.0)
$R_{\text{symm}}$ , %* †	7.9 (30.6)
Refinement (25.0–3.0 Å)	
$\sigma$ -cutoff	None
<i>R</i>	23.4 (30.7)
$R_{\text{free}}^{\ddagger}$	26.1 (34.3)
rmsd from ideal	
Bond length, Å	0.012
Bond angle, °	1.68
Average B factor, Å <sup>2</sup>	65.7

\*The number in parentheses is for the last resolution shell (3.1–3.0).

† $R_{\text{symm}} = \sum_h |I_h - \langle I \rangle| / \sum_h I$ , where  $\langle I \rangle$  is the mean intensity of reflection *h*.

‡ $R_{\text{free}}$  is for 5% of the total reflections.